

Optoacoustic Imaging of Glucagon-like Peptide-1 Receptor with a Near-Infrared Exendin-4 Analog

Sheryl Roberts¹, Eshita Khera², Crystal Choi¹, Tejas Navaratna², Jan Grimm^{1,3–5}, Greg M. Thurber^{2,6}, and Thomas Reiner^{1,4,7}

¹Department of Radiology, Memorial Sloan Kettering Cancer Center, New York, New York; ²Department of Chemical Engineering, University of Michigan, Ann Arbor, Michigan; ³Program of Molecular Pharmacology, Memorial Sloan Kettering Cancer Center, New York, New York; ⁴Department of Radiology, Weill Cornell Medical College, New York, New York; ⁵Pharmacology Program, Weill Cornell Medical College, New York, New York; ⁶Department of Biomedical Engineering, University of Michigan, Ann Arbor, Michigan; and ⁷Chemical Biology Program, Memorial Sloan Kettering Cancer Center, New York, New York

Limitations in current imaging tools have long challenged the imaging of small pancreatic islets in animal models. Here, we report the first development and in vivo validation testing of a broad-spectrum and high-absorbance near-infrared optoacoustic contrast agent, E4_{x12}-Cy7. Our near-infrared tracer is based on the amino acid sequence of exendin-4 and targets the glucagon-like peptide-1 receptor (GLP-1R). Cell assays confirmed that E4_{x12}-Cy7 has a high-binding affinity (dissociation constant, K_d, 4.6 ± 0.8 nM). Using the multispectral optoacoustic tomography, we imaged E4_{x12}-Cy7 and optoacoustically visualized β-cell insulinoma xenografts in vivo for the first time. In the future, similar optoacoustic tracers that are specific for β-cells and combines optoacoustic and fluorescence imaging modalities could prove to be important tools for monitoring the pancreas for the progression of diabetes.

Key Words: optoacoustic; diabetes; β-cell imaging; near infrared; exendin-4; sonophore; MSOT

J Nucl Med 2021; 62:839–848

DOI: 10.2967/jnumed.120.252262

Imaging does not presently play a prominent role in diabetes diagnostics. The current diagnosis for type 1 or 2 diabetes and prediabetes is based on the patient's medical history and blood screening in the form of a hemoglobin A1c test (1). However, the prevalence of diabetes is expected to drive the demand and use of molecular imaging to facilitate the diagnosis and monitoring of the disease. Type 1/2 diabetes for all age-groups worldwide is projected to rise from 171 million in 2000 to 366 million in 2030 (2). The rise in the incidence of diabetes—a major cause of blindness, kidney failure, heart attacks, stroke and lower limb amputation (3)—has not been met with a comparable, parallel refinement in diagnostic tools for its early detection. Unlike CT, MRI, ultrasonography, and intravital microscopy (4,5), which have played major roles in the field of diabetes imaging, optoacoustic imaging is thus far underrepresented among diagnostic tools. Optoacoustic glucose sensing techniques in blood and plasma samples, much

like the hemoglobin A1c test, have been reported as early as in 1999 (6). Few studies, however, focus on the newly developed techniques optoacoustic spectrometry and specific spectral unmixing algorithms intended to sense glucose (7–9). Although glucose sensing remains the most effective method for the detection of diabetes (10), the direct visualization of β-cells remains a high priority, as it promises to diagnose occult diabetes before metabolic imbalance and dysregulated blood levels manifest.

β-cells are key regulators of glucose balance via secretion of insulin, and β-cell dysfunction leads to the chronic diseases type 1 and type 2 diabetes (11,12). Prolonged high blood sugar levels can damage major organs, moreover, and lead to the development of diseases and complications beyond diabetes (13,14). Although, molecular imaging of β-cell function has always garnered interest, accurate in vivo β-cell mass identification and quantification via molecular imaging remains elusive for 3 main reasons: the first is that the tracer of choice must be specific for β-cells, the second is that β-cells make up only 1%–2% of the pancreas, and the third is that β-cells are located deep in the pancreas, which itself is located between major organs that are involved in clearance pathways (liver, spleen, and nested between parts of the gastrointestinal tract), precluding easy access for imaging. Furthermore, intravital microscopy requires invasive surgery because of light scattering, and PET requires the use of radioactive materials. Thus far, in vivo intravital imaging and PET imaging methods have played only preclinical (15–17) and early-phase clinical roles in studying the dynamic processes of pancreatic tissue (18,19).

Among other well-studied receptors (20–22), glucagon-like peptide-1 receptor (GLP-1R) is abundant on the β-cell surface and controls for blood sugar levels through insulin secretion (11,12). Since its discovery, GLP-1R has been a constant target for developing drugs. One such drug, exendin-4 (exenatide), well known for its high affinity and efficacy, is an excellent agonist (4,23). Over the past few years, several fluorescent imaging agents based on exendin-4 have been described in the literature (24–27).

Alternatively, then, noninvasive optoacoustic tomography, which combines light and sound, could represent a viable option able to image at greater depths than other optical techniques. β-cell mass identification needs a reliable method for noninvasive in vivo imaging and quantification (28,29). A handful of suitable and clinically translatable 2-dimensional (2D) and 3-dimensional (3D) handheld optoacoustic devices exist (30,31), including commercial options for clinical research (32–34). On the basis of

Received Jun. 23, 2020; revision accepted Sep. 18, 2020.
For correspondence or reprints contact, Thomas Reiner (reiner@mskcc.org).
Published online Oct. 23, 2020.
COPYRIGHT © 2021 by the Society of Nuclear Medicine and Molecular Imaging.

previous approaches and motivated by the undeniable clinical need to noninvasively resolve β -cell mass in vivo, we explored the use of exendin as a targeted vector using multispectral optoacoustic tomography (MSOT), a preclinical optoacoustic platform, similar to the equipment used in the clinics. Ideally, acoustic signals from the agent would overcome endogenous background signal against the inherently small populations of β -cells. We have shown in previous studies that several near-infrared (NIR) dyes are suitable for optoacoustic imaging (35,36). Such NIR scaffolds are characteristically high absorbers (typically $\epsilon > 200,000 \text{ cm}^{-1} \text{ M}^{-1}$) with a low quantum yield (θ) of highly packed π -conjugated aromatic systems and overlapping π -orbitals of delocalized electrons. Here, we explore the scope of NIR-exendin for applications in optoacoustic diabetes detection.

We aimed to synthesize a NIR optoacoustic sonophore, with site-specific labeling at a single position capable of targeting GLP-1R. To this end, we conjugated an exendin-4 analog to cyanine-7 (Cy7) via copper-catalyzed click chemistry, replacing the K₁₂ position of the amino acid sequence with the azide-reactive (*S*)-2-amino-4-pentynoic acid (4,26), to synthesize E4_{x12}-Cy7. To characterize E4_{x12}-Cy7, we used tissue-mimicking phantoms and mouse insulinoma xenografts that mimic normal expressions and function of GLP-1R akin to pancreatic β -cells. The research described within this article incorporates our synthetic design to target GLP-1R on the surface of β -cells using MSOT, representing the first optoacoustic visualization of insulinoma in vivo.

MATERIALS AND METHODS

General

Liquid chromatography-mass spectrometry (LC-MS) using electrospray ionization (ESI) was recorded using a Waters instrument with single-quad detector for mass identification. A lyophilizer (FreeZone 2.5 Plus; Labconco) was used for freeze drying. A BS-8000 120 V high pressure (Braintree Scientific, Inc.) multisyringe pump was used to control the flow rate and facilitate delivery of solutions inside the phantom flow system. An automated cell counter (Vi-Cell viability analyzer; Beckman Coulter) was used for counting the number of cells. In vitro fluorescence confocal microscopy was performed using a Leica TCS SP8. In vivo and ex vivo fluorescence imaging was performed using a planar (2D) IVIS Spectrum device (PerkinElmer). Pymol (1.7) was used for the 3D peptide visualization. The exendin-4 structure (identification number 3C59) was taken from the RCSB protein data bank.

Chemicals

All materials were obtained from Sigma Aldrich, unless otherwise specified. All reagents were used without further purification. Wild-type exendin-4 (H-HGEGTFTSDLSKQMEEEAVRLFIEWLKNGGPSSGAPPPS-NH₂) was purchased as a custom peptide from Innopep. Single-mutant exendin-4 (E4_{x12}) (H-HGEGTFTSXLSKQMEEEAVRLFIEWLKNGGPSSGAPPPS-NH₂), where X is the non-natural amino acid (*S*)-2-amino-4-pentynoic acid, was custom-synthesized from CSBio. Cy7 azide (no sulfate groups) was purchased from Lumiprobe.

Preparation of E4_{x12}-Cy7

Preparation and characterization of Cy7 single-mutant exendin (E4_{x12}-Cy7) was performed using azide-alkyne click chemistry. Briefly, 300 nmol of Cy7 azide were added to 100 μL of 1:1 water/*tert*-butanol containing 3 μL of CuSO₄-tris((1-hydroxy-propyl)-1H-1,2,3-triazol-4-yl)methylamine (100 mM in water) and 15 μL of L-sodium ascorbate (50 mM in water). Lastly, single-mutant E4_{x12} was added in an equal molar ratio (300 nmol) as the Cy7 azide. The

mixture was reacted under magnetic stirring for 3 h at room temperature (20 °C–25 °C). Purification was performed on a Shimadzu reverse-phase high-performance liquid chromatography system equipped with a DGU-20A 5R degasser, an SPD-20AV ultraviolet-visible light detector, a LC-6AD pump system, a CTO-20A oven maintained at 30 °C, and a CBM-20A communication bus module and using a C-18 solid-phase analytic column with a mobile phase of water (0.1% trifluoroacetic acid, buffer A) and acetonitrile (0.1% trifluoroacetic acid, buffer B). A 30%–80% CH₃CN method (gradient: 0–18 min 30%–80%, 18–20 min 80%–30%) at a flow rate of 1 mL min⁻¹ was used to separate E4₁₂-Cy7 (~16 min) from free Cy7 azide (~21 min) and unlabeled E4_{x12} (~12 min). Purified samples were lyophilized overnight, reconstituted in 1:1 water/acetonitrile, and stored at -20 °C until further use. The molecular weight of the purified product was confirmed using electrospray ionization (calculated, 4,786.39; found, 4,785.36).

Cell Culture

Mouse insulinoma-derived MIN6 cells were used between passages 13 and 17. The cells were grown in high-glucose Dulbecco modified Eagle medium containing 15% v/v heat-activated fetal bovine serum, 50 U/mL penicillin, and 10 $\mu\text{g/mL}$ streptomycin. GLP-1R-positive NIT-1 mouse cells were cultured in F12K medium supplemented with 10% (v/v) fetal bovine serum, 50 U/mL penicillin, 50 $\mu\text{g/mL}$ streptomycin, and 1.5 g/L sodium bicarbonate.

In Vitro Binding Affinity Assay

Confluent NIT-1 cells were harvested using 0.05% trypsin-ethylenediaminetetraacetic acid for 5 min before the enzymes were neutralized by adding fetal bovine serum containing F12K medium. The cells were centrifuged gently at 300 rpm for 5 min at 4 °C and resuspended in 2 mL of phosphate-buffered saline (PBS) containing 0.5% bovine serum albumin. The cells were aliquoted and incubated in triplicate with 0.5% bovine serum albumin/PBS containing E4_{x12}-Cy7 at varying concentrations (0.1–250 nM) for 3 h on ice. A control for non-specific binding was included by preincubating cells with 2 μM of unlabeled wild-type exendin on ice, followed by 0.5% bovine serum albumin/PBS containing 250 nM E4_{x12}-Cy7 and 2 μM for 3 h on ice. The cells were washed with 0.5% bovine serum albumin/PBS and analyzed by flow cytometry (ZE5 Cell Analyzer; Bio-Rad). Binding affinity (half-maximal inhibitory concentration [IC₅₀]) was estimated using GraphPad Prism, version 8, with a 1-site specific binding model.

Cell Imaging

MIN6 (1 \times 10⁵ cells/well) cells were seeded into a 96-well plate and cultured for 72 h (37 °C). The cells were then incubated with various concentrations of E4_{x12}-Cy7 for 90 min at 37 °C alone or with exendin-4 (500 nM) coincubated with various concentrations of E4_{x12}-Cy7 (25–100 nM) for 90 min at 37 °C. After incubation, the cells were washed once with 200 μL of PBS and fixed by adding 100 μL of 4% paraformaldehyde and allowed to sit at room temperature for 15 min. Paraformaldehyde was removed and washed with PBS (200 μL , 3X). The cells were mounted on PBS with NucSpot 488 and imaged with a confocal fluorescence microscope (TCS SP8; Leica).

Tissue-Mimicking Phantom Preparation and Experimental Setup

A phantom mold was prepared to fit the MSOT holder. The phantom allows for a flow-mediated setup as previously shown (35). Briefly, a clear, cylindric hollow membrane tubing was placed at the center of a cylindric mold (20-mL syringe; diameter, 2 cm; length, 14 cm). The soft-tissue-mimicking phantom was freshly prepared by adding 15% v/v intralipid 20% I.V. (Fresenius Kabi AB) fat emulsion (to

provide the scattering), and 0.01 mM direct red 81 (for absorption) to a prewarmed solution of 5% v/v agarose type 1 (solid in <37 °C) in Milli-Q water (Millipore Corp.) (18.2 MΩ cm⁻¹ at 25 °C). At 15% agarose, the phantom was suspended in water, with the weight of the hollow tubing being supported. The mixture was poured into the mold and allowed to cool and solidify for at least 2 h and up to overnight at 4 °C. At each end of the tubing, a Luer-lock was fitted to connect the syringe pump, equipped with a 20-mL syringe filled with PBS. Air gaps were used to separate the sample and PBS. The flow rate was kept at 1 mL min⁻¹ until the sample of interest reached the region of interest (ROI) for imaging. After imaging, the flow rate was increased 2 times and the phantom was washed with at least 10 mL of PBS. The wash, load sample, and wash cycle were repeated for all samples. The flow-mediated phantom setup sustained several acquisitions throughout the day, and the same phantom setup was used for all samples that were compared with each other.

MSOT

An MSOT inVision device (version 256; iThera Medical) for small-animal imaging was used. MSOT inVision has an array of 256 detector elements that are cylindrically focused, with a central ultrasound frequency of 5 MHz and up to 270° of coverage. The soft-tissue-mimicking phantoms were aligned so that the illumination ring coincided with the detection plane, that is, the curved transducer array was centered around the phantom. Data were obtained in the wavelength range of 680–900 nm (10-nm increments), and an average of 10 frames per wavelength were acquired, which equates to a 1-s acquisition time per wavelength per section. The optical excitation originates from a Q-switched neodymium-doped yttrium aluminum garnet laser with a pulse duration of 10 ns and a frequency of 10 Hz. Light is homogeneously delivered to the phantom using a fiber split into 10 output arms. The fiber bundle and the transducer array are stationary, and the sample holder moves along the z-direction, allowing longitudinal acquisition of different imaging planes using a moving stage. MSOT measurements were performed in a temperature-controlled water bath at 34 °C. All variable parameters such as optoacoustic gain, laser power, focus depth, frame averaging, frame rate, and high- or low-pass filters were kept constant during the measurement. Samples were allowed to equilibrate for a minimum of 5 min before the optoacoustic scan was initiated, and the concentrations of E4_{x12}-Cy7 were 2, 5, 10, 15, and 25 μM in 0.9% sodium chloride. Sample solutions were delivered to the center of the phantom using a syringe pump. Between the measurements, the flow device was washed with deionized water (>10 mL).

Optoacoustic Image Data Processing

Spatial reconstruction and multispectral processing of the data were performed using the ViewMSOT software suite (version 3.6; iThera Medical) and a backprojection algorithm. The normalized optoacoustic spectra were obtained from optoacoustic phantom scans taken from a 25 μM sample and used as a contrast agent reference. For multispectral unmixing, a linear regression method was used and excluded pixels where the number of wavelengths (>25%) fell within the negative signal. Hemoglobin and deoxyhemoglobin reference spectra included in the software package were used for multispectral unmixing. MIN6 cells were implanted in the same position and distance from the surface of the skin across animals. Hence, all animals are affected to the same degree by light scattering. Quantitative information was obtained by defining the ROI manually within a 2D MSOT image. For spectrally unmixed E4_{x12}-Cy7, the mean pixel intensities per cross-section in the volume of interest were first plotted as classic least square score versus position (mm) to assess its signal strength. Signal strength is decreasing with distance from the xenograft and creating a parabolic shape. The maximum “mean signal per cross-section” was used as a

quantitative indicator of the probe binding. Overall optoacoustic intensities (arbitrary units) were reported at all imaging wavelengths (680–900 nm, 10-nm step resolution). For all cases, unless otherwise stated, the classic least square method for spectral deconvolution was used and reported as classic least square scores. The following reference spectra were used: hemoglobin, deoxy-hemoglobin, and E4_{x12}-Cy7. To compare the direct intensities of all images, the optoacoustic spectrum (25 μM) was normalized to their maximum optoacoustic (760 nm) wavelength. The channel for E4_{x12}-Cy7 (green) after multispectral unmixing was overlaid with the overall optoacoustic intensities (arbitrary units, bone scale).

Animal Studies

All animal experiments were performed in accordance with protocols approved by the Institutional Animal Care and Use Committee of Memorial Sloan Kettering Cancer Center and followed the National Institutes of Health guidelines for animal welfare. Healthy Hsd:athymic female mice NudeFoxn1tm (6–8 wk old) were obtained from the Jackson Laboratory. The mice were split into 2 groups of 3 mice, with one group being injected with the imaging agent and the other being used as a noninjected control group. All animal procedures, other than tail vein injections, were performed with the animals under general 1.5%–2% isoflurane inhalation anesthesia. To test GLP-1R receptor specificity, xenografts were created using the pancreatic mouse insulinoma line MIN6. MIN6 cells were injected into the right flank (1 × 10⁶ cells in 50 μL of 1:1 Dulbecco Eagle medium high-glucose [DMEM HG] and Matrigel [Corning]). The xenografts were left for 12–15 days to allow for proper vasculature formation around the β-cell clusters before imaging. From MSOT imaging, the mice were placed into the animal holder in supine position, gently fixed into position using clear straps, and fitted with a breathing mask for anesthesia. Ultrasound colorless gel (approximately 1- to 2-mm-thick layer) was applied onto the mouse around the ROI to improve acoustic coupling. The animal holder was closed, wrapping the clear plastic membrane around the mouse and removing air gaps and bubbles between the membrane and the mouse's skin. The animal holder with the mouse positioned inside it was then placed into the imaging chamber, with the animal being aligned with regard to the detection plane (centered within the curved transducer array). MIN6-bearing mice (*n* = 3) were imaged with the MSOT before injection. Group 1 mice were injected via the tail vein with 100 μL of 2.9 mM kg⁻¹ E4_{x12}-Cy7. The mice were reimaged at 30 min after injection. E4_{x12}-Cy7 was dissolved in 0.9% sodium chloride solution. Animals were also imaged in tandem using an IVIS Spectrum (PerkinElmer) system for planar fluorescence imaging.

Blocking In Vivo Experiments

MIN6-bearing mice were split into 3 groups, namely saline, blocking, and E4_{x12}-Cy7-injected groups (*n* = 3). The saline group was injected with 100 μL of 0.9% sodium chloride; the blocking group was injected with 151 μg of exendin-4 (100 μL of 360 μM) and allowed to circulate for 30 min, followed by injection of 57 μg of E4_{x12}-Cy7 (100 μL of 120 μM); and E4_{x12}-Cy7 group was injected with 100 μg of E4_{x12}-Cy7 (100 μL of 120 μM). The mice were imaged before and after injections using the epifluorescence IVIS Spectrum system and the MSOT.

Ex Vivo Imaging of Tissues

Thirty minutes after intravenous injection and optoacoustic imaging, kidney, liver, pancreas, spleen, muscle, and MIN6 cluster were harvested and planar fluorescence imaging was performed.

Statistical Analysis

Paired *t* tests were performed to determine statistical difference in vivo before and after injection. The levels of significance were *P* values of less than 0.05, 0.01, 0.001 and 0.0001. Data are presented as mean ± SD.

RESULTS

Synthesis and Analysis of E4_{x12}-Cy7

A GLP-1R-targeted peptide, exendin-4, was modified at the K₁₂ position of the amino acid sequence with the unnatural alkyne-amino acid (*S*)-2-amino-4-pentynoic acid (Fig. 1A). As reported previously (4,24,26), it can be used without a significant reduction of peptide/GLP-1R target binding (~3 nM) (4). Likewise, we have previously shown that cyanine dyes such as Cy7 exhibit the desired optical characteristics suitable for both optoacoustic and fluorescent imaging (36). The synthesis of E4_{x12}-Cy7 was achieved in a 1-step reaction (Fig. 1B). Cy7-azide was used for labeling of the neopeptide E4_{x12} (gray) via a bioorthogonal copper(I)-catalyzed azide-alkyne cycloaddition reaction to obtain E4_{x12}-Cy7 (Fig. 1B, bottom) in good yield (>90%) and purity (78%; tR [retention time] = 12.15 min; Fig. 1C). The targeting peptide exendin-4, neopeptide E4_{x12}, and the optoacoustic agent E4_{x12}-Cy7 are amino acid sequences consisting of 39 amino acids (Fig. 1A). E4_{x12}-Cy7 has a broad absorption, ranging from 550 to 850 nm, with a maximum absorption at 760 nm, indicating an appropriate wavelength range for multispectral optoacoustic unmixing (37). Mass spectrometry confirmed the identity of E4_{x12}-Cy7 (Fig. 1D).

Validation of E4_{x12}-Cy7 as an Optoacoustic Agent in Tissue-Mimicking Phantom

The MSOT inVision 256 was used to measure optoacoustic signals. A flow device, fitted into the commercially available MSOT imaging system and containing a soft-tissue mimicking phantom, was prepared as previously described in detail (35,36). To evaluate

the optoacoustic performance of E4_{x12}-Cy7, solutions of E4_{x12}-Cy7 in DMSO at concentrations between 2 and 25 μM were prepared. Using a syringe pump, the samples were allowed to flow at roughly 1 mL/min until they reached the middle of the phantom. The observed optoacoustic spectrum of E4_{x12}-Cy7 was broad at all of the measured concentrations (Fig. 2A, left), with optoacoustic maxima at 760 nm (Fig. 2A, middle), in agreement with the absorbance maxima at 760 nm (Fig. 1C). The optoacoustic spectrum at 25 μM was used as the reference spectrum for MSOT spectral unmixing. After spectral unmixing, there was a linear correlation between the optoacoustic signal and the concentration of E4_{x12}-Cy7 ($R^2 = 0.99$; Fig. 2A, right). Representative 2D optoacoustic images of the phantom with the E4_{x12}-Cy7 at varying concentrations were reconstructed, and 900 nm was chosen as the representative optoacoustic background (Fig. 2B). A linear regression fitting algorithm using classic least square (CLS) of known spectra was used to unmix the raw optoacoustic data (arbitrary units), and the algorithm produces a classic least square score (38–40). In our case, 3 references were included and used for spectral unmixing of hemoglobin, deoxyhemoglobin, and E4_{x12}-Cy7.

Binding, Affinity, and Inhibition

Cell assays were performed using MIN6 cells and NIT-1 cells; both were derived from mouse pancreatic β-cell insulinomas. E4_{x12}-Cy7 is both an optoacoustic agent and a fluorescent agent, with a dissociation constant, K_d, of 4.6 ± 0.8 nM (Fig. 3A). In general, concentrations lower than 50 nM produced the best results, likely due to self-quenching of the tracer at higher concentrations. Incubation of E4_{x12}-Cy7 below 50 nM concentration

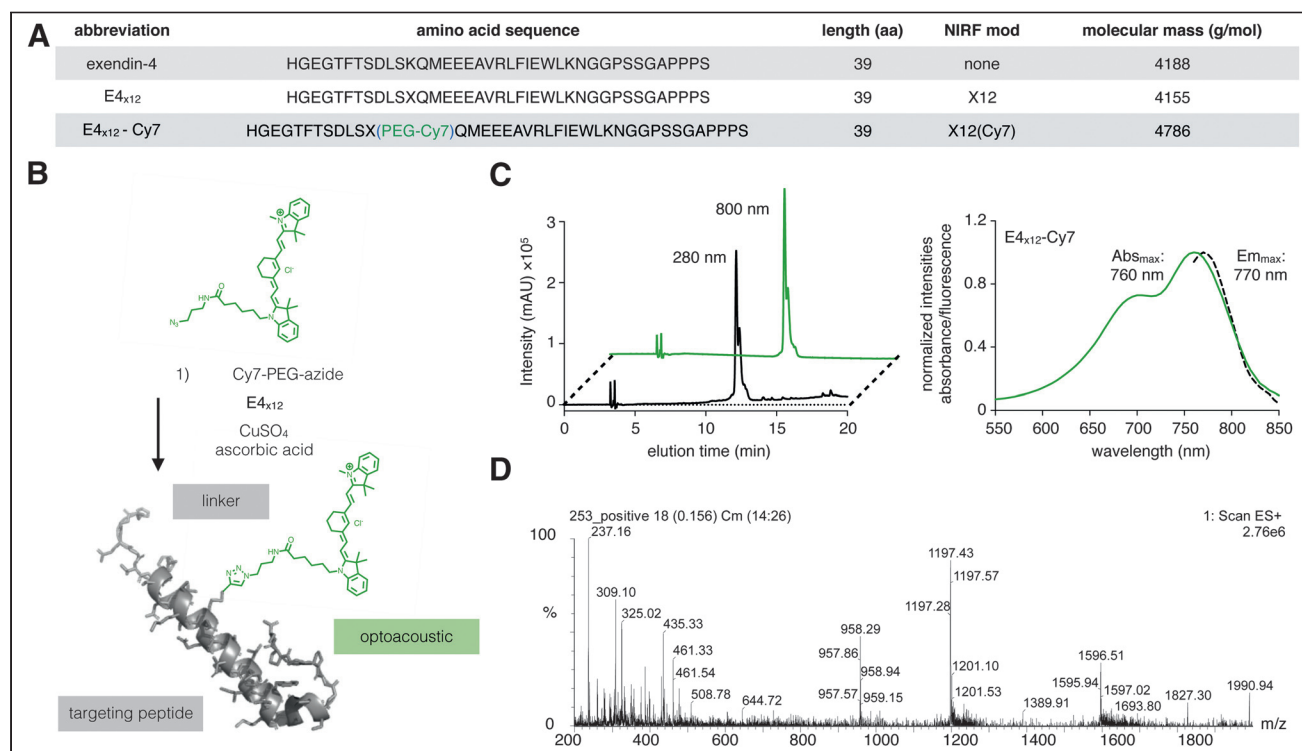


FIGURE 1. Synthesis and analysis of E4_{x12}-Cy7. (A) Abbreviations and amino acid sequences of exendin-4 and its modified derivatives. (B) Copper-catalyzed azide-alkyne cycloaddition reaction scheme yielding optoacoustic probe E4_{x12}-Cy7. (C) High-performance liquid chromatography trace, 5%–95% MeCN: 15-min linear gradient (left) and absorbance/emission spectra (right) of E4_{x12}-Cy7. (D) Electrospray ionization mass spectrometry spectrum of E4_{x12}-Cy7. Abs_{max} = absorbance max; Em_{max} = emission max; ES+ = electrospray ionization; m/z = mass-to-charge ratio; NIRF mod = NIR fluorescence modification.

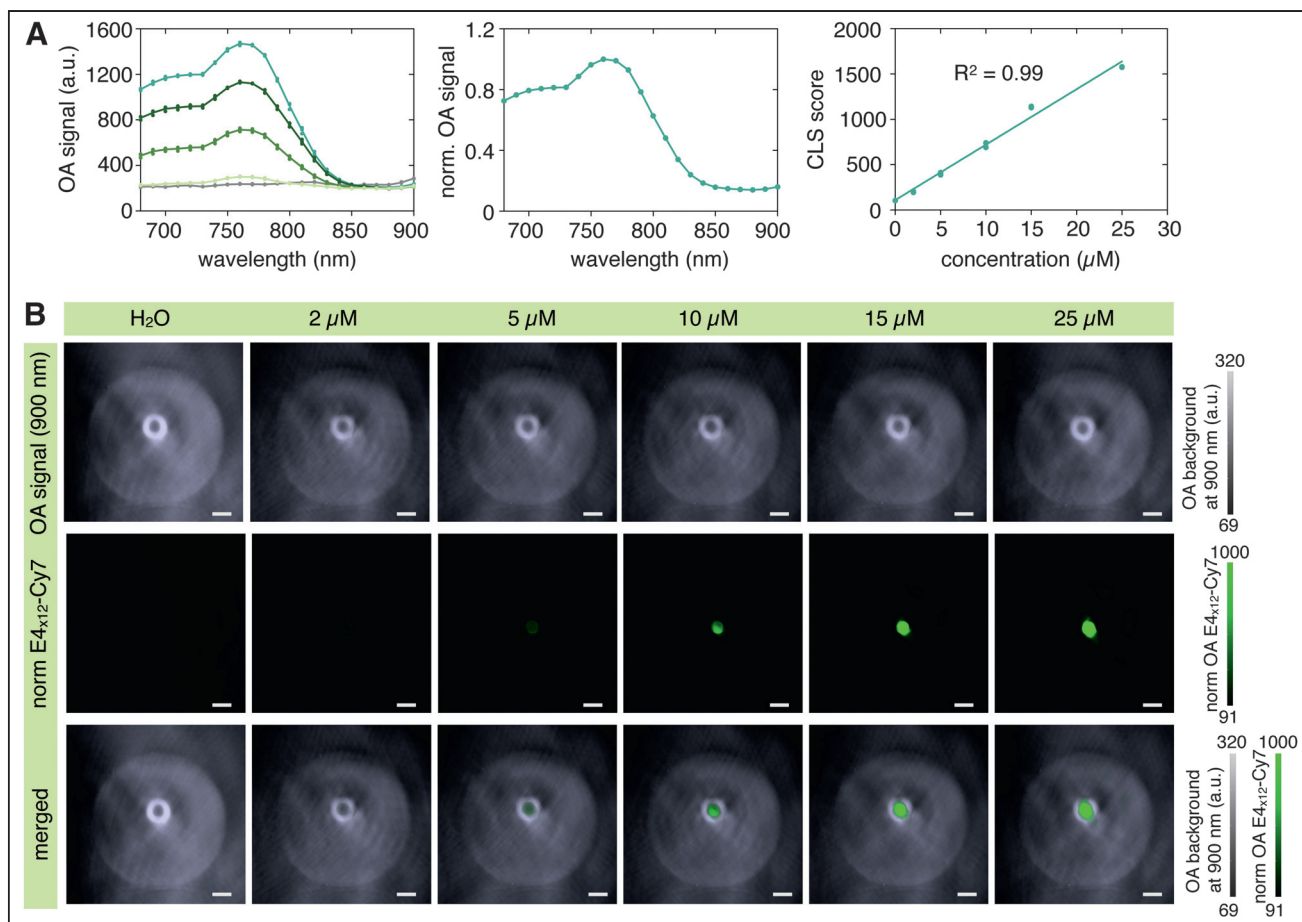


FIGURE 2. Evaluation of pancreatic β -cell-targeting peptide ($E4_{x12}$ -Cy7) as optoacoustic probe in soft-tissue-mimicking phantoms. (A, left) Optoacoustic spectra at 680–900 nm with 10-nm wavelength resolution at various concentrations of $E4_{x12}$ -Cy7 (2, 5, 10, 15, and 25 μ M). (A, middle) Normalized spectrum (25 μ M) at maxima optoacoustic signal. (A, right) Optoacoustic signal at various concentrations obtained after multispectral unmixing. (B) Optoacoustic image reconstruction of $E4_{x12}$ -Cy7 solutions embedded in homogeneous and absorbing soft-tissue-mimicking phantom. CLS = classic least square; norm = normalized; OA = optoacoustic. Scale bars are 2.5 mm.

regimes using MIN6 cells showed a relative increase in fluorescence with increasing concentrations (Supplemental Fig. 1A; supplemental materials are available at <http://jnm.snmjournals.org>). Incubation of $E4_{x12}$ -Cy7 at 50 nM in the MIN6 cell line proved to be the optimal concentration for fluorescence imaging (Fig. 3B). To test the specificity of $E4_{x12}$ -Cy7 for GLP-1R, we coinubated MIN6 cells with non-fluorescent exendin-4 (500 nM) and varying concentrations of $E4_{x12}$ -Cy7 (Supplemental Fig. 1B). Coincubation of exendin-4 (500 nM, 5- to 20-fold excess) relative to $E4_{x12}$ -Cy7 produced no fluorescence uptake within the cells (Supplemental Fig. 1B). These results showed that $E4_{x12}$ -Cy7 was taken up specifically via by GLP-1R and that its uptake could be inhibited completely by the presence of excess unlabeled peptide. Binding of $E4_{x12}$ -Cy7 to the GLP-1R induced internalization resulting in cytosolic as well as membrane localization at 90 min of incubation.

GLP-1R-Mediated Accumulation of $E4_{x12}$ -Cy7

After MSOT preimaging sessions, mice used for blocking experiments were injected with 151 μ g of exendin-4 (100 μ L, 360 μ M, 30-min interval) before intravenous injection with 57 μ g of $E4_{x12}$ -Cy7 (100 μ L, 120 μ M, 30-min interval), and MSOT imaging was performed. Likewise, mice that were injected with saline or 57 μ g of $E4_{x12}$ -Cy7 were imaged before and 20 min after injections. Ex

vivo biodistribution via fluorescence imaging showed that the kidney has the highest accumulation of $E4_{x12}$ -Cy7 (Supplemental Fig. 2). An ROI drawn around the kidney before and after MSOT in vivo imaging (Fig. 4A) showed that the optoacoustic spectral profile matched that of $E4_{x12}$ -Cy7 (Fig. 2A, left/right). As a reference point, an ROI around an area that is not kidney was also plotted as background. Therefore, there can be no doubt that the signal after spectral unmixing was from the Cy7 dye. When imaging the kidneys ex vivo with MSOT, a statistically significant difference between saline-injected mice and $E4_{x12}$ -Cy7 was observed ($P = 0.0178$; Supplemental Fig. 3). To confirm further, the organs from the pancreas, muscle, and insulinoma MIN6 were immediately harvested and imaged with the MSOT (Fig. 4B). A statistically significant difference between muscle and the pancreas ($P < 0.0001$) and between the muscle and MIN6 ($P < 0.0001$) were observed (unpaired t test). In addition, in vivo epifluorescence imaging showed a statistically significant difference between the blocking and $E4_{x12}$ -Cy7 groups ($P = 0.0042$), showing that the signal was blockable (Fig. 4C). Moreover, organs (insulinoma MIN6, pancreas, muscle, kidney, spleen, and liver) were excised and placed side by side on a black nonfluorescent paper. Epifluorescence imaging was performed, ROIs were drawn around the edges of the organs, and the average fluorescence signal was calculated. The signal originating from the mouse

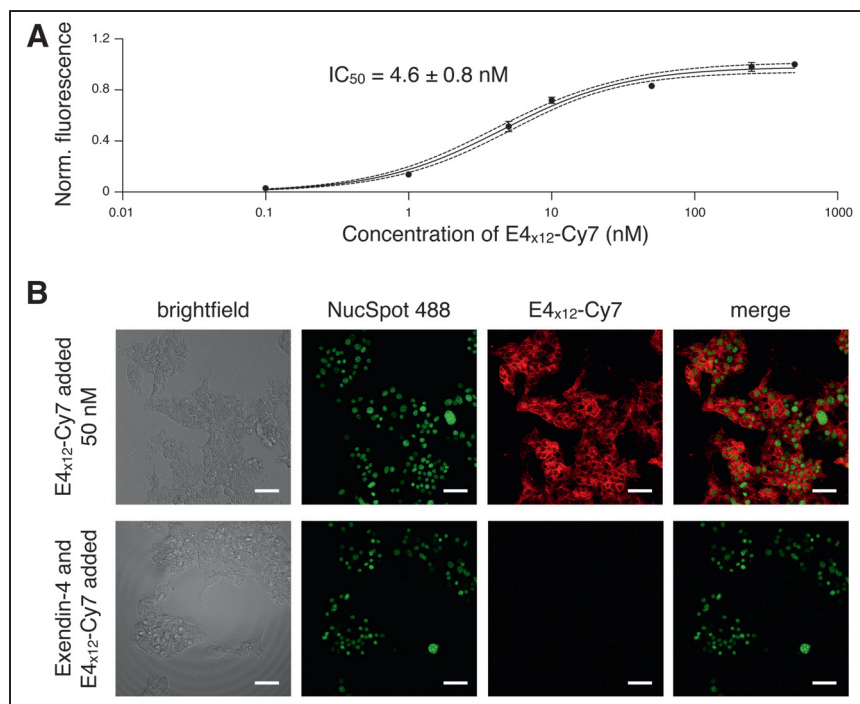


FIGURE 3. In vitro binding and inhibition studies. (A) Dissociation constant, K_d , of $E4_{x12}$ -Cy7 measured via competitive binding assay using NIT-1 cells. (B) Confocal microscopy imaging experiments using MIN6 cells after addition of $E4_{x12}$ -Cy7 (top) or after coincubation with excess exendin-4 (bottom). From left to right is brightfield image, image showing nuclear staining with NucSpot 488, and image showing 50 nM $E4_{x12}$ -Cy7 staining or coincubation with excess exendin-4 and its composite. IC_{50} = half-maximal inhibitory concentration. Scale bars are 40 μ m.

insulinoma MIN6 was statistically significant ($P = 0.0199$) between the blocking and $E4_{x12}$ -Cy7 groups (Fig. 4D).

Optoacoustic Imaging of Insulinoma

MIN6 cells were used in a mouse model of pancreatic insulinoma because they closely resemble pancreatic β -cells, including their GLP-1R expression and insulin secretion (37,41). To determine specific optoacoustic detection and optoacoustic imaging of insulinoma xenografts in vivo, mice were intravenously injected with 57 μ g of $E4_{x12}$ -Cy7. MSOT imaging of the same mice before injection served as the negative control. Optoacoustic imaging using the MSOT before and 30 min after administration showed a statistically significant increase in signal within the tumors (Fig. 5A). Mice that were imaged 30 min after intravenous injection of $E4_{x12}$ -Cy7 had an optoacoustic signal score of 72.69 ± 2.72 ($n = 3$ mice). Pre-injected mice had an optoacoustic background signal score of 30.54 ± 1.80 ($n = 3$ mice; Fig. 5B). Optoacoustic signal showed a statistically significant difference in mouse insulinoma signal before and after intravenous injection of $E4_{x12}$ -Cy7 ($P = 0.0236$). The signal strength ratio between the injected and noninjected mice was found to be 2.38 (Fig. 5B). In addition, fluorescence imaging in vivo and ex vivo was performed (Supplemental Fig. 2). Fluorescence imaging corroborated our optoacoustic imaging observations. Ex vivo analysis of $E4_{x12}$ -Cy7 showed uptake in the kidney and liver as well (Supplemental Fig. 2).

DISCUSSION

Optoacoustic technologies are quickly gaining increasing relevance in diagnostics, tracking disease progression, as well as

evaluating treatment therapies through imaging of disease-relevant biologic processes (42). For this application, the most attractive feature of MSOT over other optoacoustic systems is its ability to provide molecular information, including a range of wavelength measurements in the NIR region that enable multi-spectral unmixing between endogenous and exogenous contrast agents. Hence, a highly absorbing NIR agent, such as our $E4_{x12}$ -Cy7, can achieve sufficient contrast for in vivo β -cell detection. Compared with traditional fluorescence imaging systems, the key difference of MSOT is that its ability to use light for excitation and sound for detection enables a greater penetration depth. The development of optoacoustic imaging tools for diabetes is a valuable but unmet clinical need (7,8,25,31,43). A handful of proof-of-concept studies in the literature has emerged to show the potential of diabetes monitoring via optoacoustic imaging, but none feature direct visualizations of β -cells (6–9,19,44–46).

Recent studies typically demonstrated an indirect biologic response to the symptoms of diabetes via vasculature tracking (44,47), diabetic neuropathy (48), or glucose sensing (8,45,46). And although CT, MRI, ultrasonography and intravital microscopy (4) are well established in the field of pre-clinical diabetes imaging, the techniques are hampered by photon absorption and scattering in tissues. Here, an optoacoustic agent, $E4_{x12}$ -Cy7, was successfully synthesized, purified, chemically and optoacoustically characterized, and validated in vitro and in vivo. A promising sonophore has a high extinction coefficient and broad absorption profile (36), which initially led to our rationale behind Cy7 as the absorber of choice for conjugating to neopeptide $E4_{x12}$. The introduction of an optoacoustic tracer, Cy7, to the 12th position of the amino acid sequence did not perturb its binding affinity to GLP-1R, similar to what we found earlier when substituting at the 14th position (4,49). $E4_{x12}$ -Cy7 maintained its high receptor binding and cellular internalization at 90 min after incubation and proved to be receptor-specific, since it was blocked by a 5- to 20-fold excess of exendin-4.

For in vivo imaging, we chose GLP-1R-expressing mouse insulinoma MIN6, derived from transgenic mice and preserving the normal characteristics and function of the endocrine β -cells (37). In vivo, healthy 6- to 8-week-old Fox1ⁿ nude MIN6-bearing mice were injected with $E4_{x12}$ -Cy7. Intravenous injection of $E4_{x12}$ -Cy7 showed specific uptake after 30 min, which we were able to detect with both MSOT and fluorescence imaging in the same animal. Cy7 has a broad optoacoustic spectra with a maximum at 760 nm. A similar optoacoustic spectral profile was obtained in the kidney regions after intravenous injection, confirming the presence of $E4_{x12}$ -Cy7 in vivo. This profile was further corroborated with ex vivo MSOT imaging of the corresponding organs of interest. This signal was blockable with exendin-4. To test $E4_{x12}$ -Cy7, in vivo imaging was performed on mice with subcutaneous MIN6

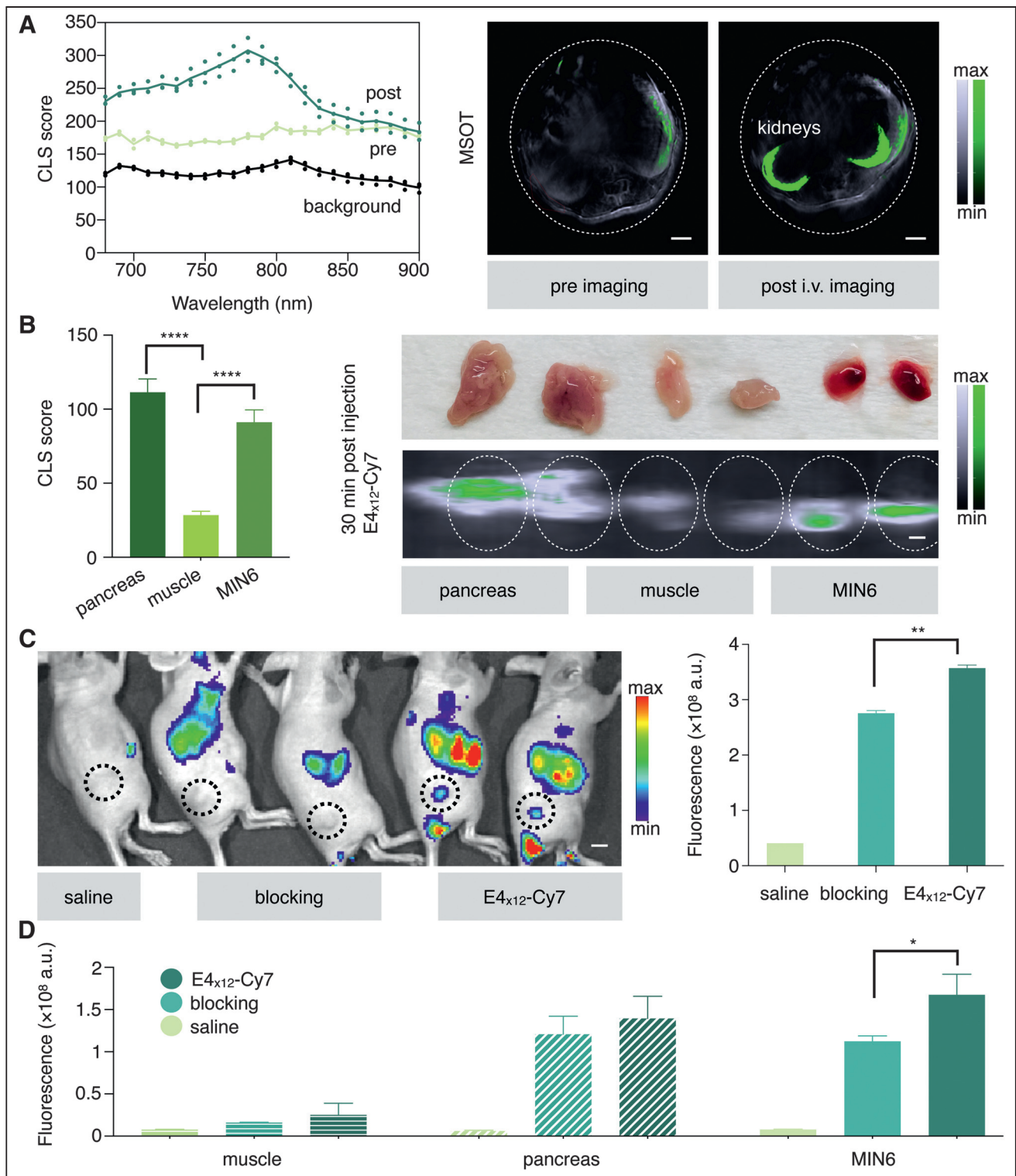


FIGURE 4. GLP-1R-mediated accumulation of E_{4x12} -Cy7. (A) Optoacoustic signal at varying wavelengths (680–900 nm, 10-nm steps) taken at kidney region (left) and corresponding MSOT images (right). Scale bars are 2.5 mm. (B) Ex vivo MSOT images of organs (pancreas, muscle, and MIN6) from mice that were injected with E_{4x12} -Cy7 (right) and corresponding quantification (left). Scale bar is 2.5 mm. (C) Representative in vivo epifluorescent images of mice that were injected with saline, mixture of exendin-4 and E_{4x12} -Cy7 (3:1 ratio), or E_{4x12} -Cy7 (left) and in vivo quantification (right). Scale bar is 0.79 cm. (D) Quantification from epifluorescent images of ex vivo muscle, pancreas, and MIN6. Ex vivo organs correspond to mice that were injected with saline, mixture of exendin-4 and E_{4x12} -Cy7 (3:1 ratio), or E_{4x12} -Cy7 (left to right). a.u. = arbitrary units; CLS = classic least square; i.v. = intravenous.

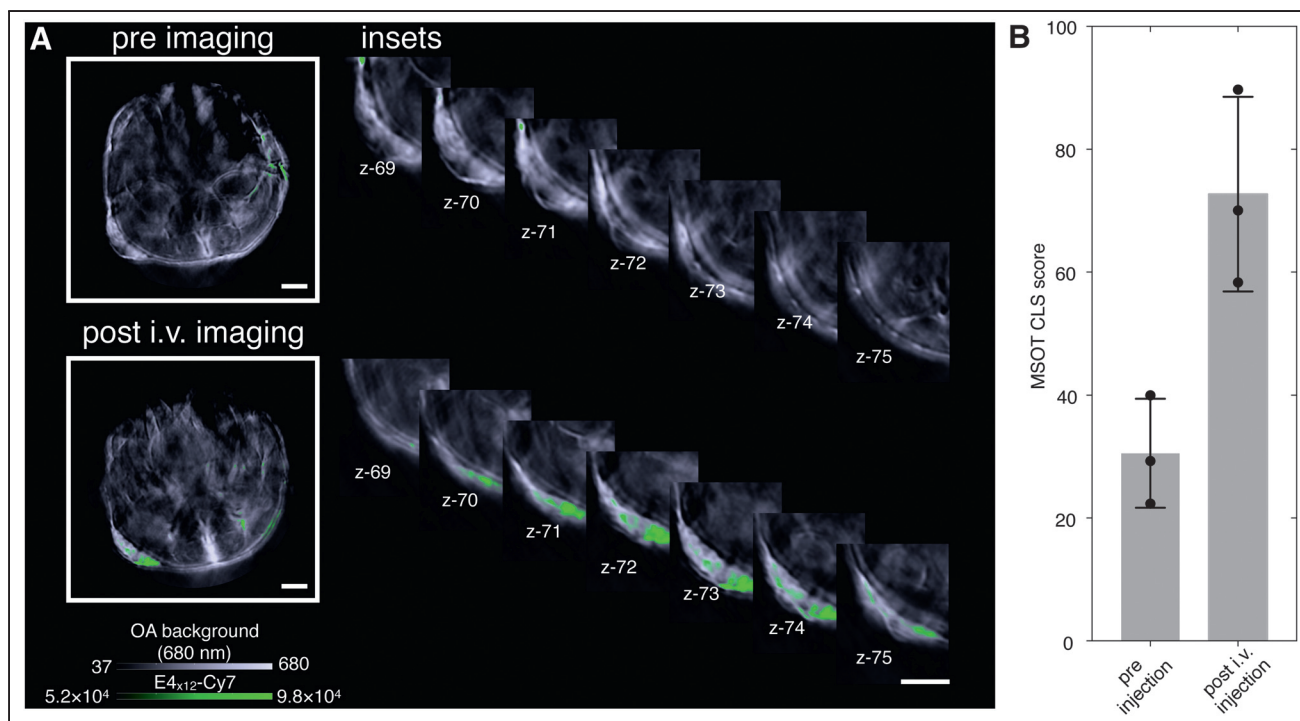


FIGURE 5. In vivo multispectral optoacoustic evaluation of E4_{x12}-Cy7. (A) Optoacoustic image reconstruction showing transverse 2D projection of mice at ROI before and 30 min after intravenous injection of E4_{x12}-Cy7 (2.9 mg/kg). After multispectral unmixing, E4_{x12}-Cy7 channel (green) was overlaid on overall optoacoustic signal at 680 nm (grayscale). All scale bars are 2.5 mm. (B) Optoacoustic signal quantification after multispectral unmixing. CLS = classic least square; i.v. = intravenous; OA = optoacoustic.

insulinomas. This model was chosen as our focus to limit biologic variability, reducing the complexity that comes with imaging the pancreas. Initially, visualization of a solid subcutaneous mass of β -cells is much easier than visualization of the 1%–2% of β -cells that are spread throughout the pancreas. Moreover, we are minimizing the physiologic challenges that exists when imaging mouse pancreata. In mice, a pancreas is rather flat and dendrite-like, whereas in humans, it is a well-defined solid mass. Nevertheless, we have also demonstrated uptake in the pancreas. This is expected since approximately 2.4×10^5 β -cells are found in the pancreas of a 10-week-old mouse (50) and we injected 1×10^6 MIN6 cells. This may be a reason for the signal uptake in the pancreas to appear as high as in the subcutaneous MIN6 model. In our model, we have observed rapid clearance after 30 min after intravenous injection of E4_{x12}-Cy7 (Supplemental Fig. 4), possibly because of the short half-life (1–2 min) of GLP-1 caused by N-terminal degradation by the enzyme dipeptidyl peptidase-4 (51). Although the high extinction coefficient of Cy7 dye ($206,000 \text{ M}^{-1} \text{ cm}^{-1}$) is adequate for optoacoustic imaging, we suspect its fluorescent nature may not be optimal as an imaging agent for MSOT. Taken together, this could potentially be a limitation and leaves room for further development of other optoacoustic β -cell targeting agents.

Exendin-4 allows for a modular design without perturbing its affinity to GLP-1R. Here, we have shown the first (to our knowledge) development and in vivo validation of a NIR MSOT agent, E4_{x12}-Cy7, an exendin-4 analog that binds to GLP-1R. In our in vitro and in vivo blocking studies using native peptide exendin-4, we showed that the modified sonophore retained its targeting profile of exendin-4. The MSOT can achieve multispectral unmixing methods, which deliver specific information from E4_{x12}-Cy7. Consequently, E4_{x12}-Cy7 could work well with the hand-held

optoacoustic imaging system. In addition, the incorporation of 3D optoacoustic tomographic systems could work favorably with NIR absorbers, known to provide more quantitative assessments (30). On the basis of the previous success of specific β -cell imaging agents for PET, fluorescence imaging, or combinations thereof (4,24,26), we envision that a contrast agent such as E4_{x12}-Cy7 could represent a potential platform for further development and optimization of β -cell optoacoustic imaging.

CONCLUSION

In this study, we synthesized and characterized E4_{x12}-Cy7, an optoacoustic imaging agent based on exendin-4, a first-generation GLP-1R-targeted optoacoustic β -cell agent. Using MSOT, E4_{x12}-Cy7 showed specific uptake for MIN6 xenografts. The high spatial resolution and penetration depth achieved with MSOT, in combination with targeted NIR E4_{x12}-Cy7, could represent a valuable technique for monitoring diabetes and its progression in both pre-clinical and clinical contexts. This study is the first step toward the development of β -cell mass optoacoustic imaging, a technique that merits further investigation as the already enormous challenge diabetes represents continues to grow.

DISCLOSURE

This work was supported by National Institutes of Health grants R01 CA204441 (Thomas Reiner), R01 CA212379 (Jan Grimm), R35 GM128819 (Greg Thurber), and P30 CA008748. Thomas Reiner is a shareholder of Summit Biomedical Imaging, LLC. Jan Grimm and Thomas Reiner are coinventors on a filed U.S. patent (US20190275179A1) that covers optoacoustic imaging agents. Thomas Reiner is a coinventor on a U.S. patent (WO2012121746A2)

covering the composition of matter for islet imaging agents. Thomas Reiner is a paid consultant for and has received grant support from Theragnostics, Inc. No other potential conflict of interest relevant to this article was reported.

ACKNOWLEDGMENTS

For their support, we thank Memorial Sloan Kettering Cancer Center Animal Imaging Core Facility, Radiochemistry and Molecular Imaging Probes Core Facility, Molecular Cytology Core Facility, and Nuclear Magnetic Resonance Analytical Core Facility and the University of Michigan Flow Cytometry Core Facility. We thank Christopher Wittman for assistance with cell cultures during the revision of the paper and Garon Scott for proofreading the manuscript.

KEY POINTS

QUESTION: Is optoacoustic imaging of the GLP-1R possible with a first-generation NIR exendin-4 analog, E_{4x12}-Cy7?

PERTINENT FINDINGS: E_{4x12}-Cy7, a novel optoacoustic imaging probe, targets the GLP-1R on the surface of β -cells in a pancreatic mouse model of insulinoma. E_{4x12}-Cy7 was successfully synthesized and showed high binding affinity comparable to exendin-4. MSOT with E_{4x12}-Cy7 allowed in vivo optoacoustic imaging of GLP-1R, which was blockable.

IMPLICATIONS FOR PATIENT CARE: A NIR E_{4x12}-Cy7 and similar analogs can be exploited for MSOT imaging, combining capabilities of both light for excitation and sound for detection that could prove to be important contrast agents for monitoring the pancreas for the progression of diabetes.

REFERENCES

- American Diabetes Association. 2. Classification and Diagnosis of Diabetes: Standards of Medical Care in Diabetes—2018. *Diabetes Care*. 2018;41(suppl):S13–S27.
- Wild S, Roglic G, Green A, Sicree R, King H. Global prevalence of diabetes: estimates for the year 2000 and projections for 2030. *Diabetes Care*. 2004;27:1047–1053.
- Rowley WR, Bezold C, Arikian Y, Byrne E, Krohe S. Diabetes 2030: insights from yesterday, today, and future trends. *Popul Health Manag*. 2017;20:6–12.
- Reiner T, Thurber G, Gaglia J, et al. Accurate measurement of pancreatic islet β -cell mass using a second-generation fluorescent exendin-4 analog. *Proc Natl Acad Sci USA*. 2011;108:12815–12820.
- Reiner T, Kohler RH, Liew CW, et al. Near-infrared fluorescent probe for imaging of pancreatic beta cells. *Bioconjug Chem*. 2010;21:1362–1368.
- MacKenzie HA, Ashton HS, Spiers S, et al. Advances in photoacoustic noninvasive glucose testing. *Clin Chem*. 1999;45:1587–1595.
- Dasa MK, Markos C, Janting J, Bang O. Multispectral photoacoustic sensing for accurate glucose monitoring using a supercontinuum laser. *J Opt Soc Am B*. 2019;36:A61–A65.
- Ghazaryan A, Ovsepian SV, Ntziachristos V. Extended near-infrared optoacoustic spectrometry for sensing physiological concentrations of glucose. *Front Endocrinol (Lausanne)*. 2018;9:112.
- Zhang R, Gao F, Feng X, et al. “Guide star” assisted noninvasive photoacoustic measurement of glucose. *ACS Sens*. 2018;3:2550–2557.
- Bruen D, Delaney C, Florea L, Diamond D. Glucose sensing for diabetes monitoring: recent developments. *Sensors (Basel)*. 2017;17:1866–1888.
- Pattou F, Kerr-Conte J, Wild D. GLP-1-receptor scanning for imaging of human beta cells transplanted in muscle. *N Engl J Med*. 2010;363:1289–1290.
- Jones B, Buenaventura T, Kanda N, et al. Targeting GLP-1 receptor trafficking to improve agonist efficacy. *Nat Commun*. 2018;9:1602–1619.
- Raptis AE, Markakis KP, Mazioti MC, Raptis SA, Dimitriadis GD. What the radiologist needs to know about the diabetic patient. *Insights Imaging*. 2011;2:193–203.
- Vetere A, Choudhary A, Burns SM, Wagner BK. Targeting the pancreatic β -cell to treat diabetes. *Nat Rev Drug Discov*. 2014;13:278–289.
- van Gurp L, Loomans CJM, van Krieken PP, et al. Sequential intravital imaging reveals in vivo dynamics of pancreatic tissue transplanted under the kidney capsule in mice. *Diabetologia*. 2016;59:2387–2392.
- Coppieters K, Amirian N, von Herrath M. Intravital imaging of CTLs killing islet cells in diabetic mice. *J Clin Invest*. 2012;122:119–131.
- Brom M, Joosten L, Frielink C, et al. Validation of ¹¹¹In-exendin SPECT for the determination of the β -cell mass in BioBreeding diabetes-prone rats. *Diabetes*. 2018;67:2012–2018.
- Luo Y, Pan Q, Yao S, et al. Glucagon-like peptide-1 receptor PET/CT with ⁶⁸Ga-NOTA-exendin-4 for detecting localized insulinoma: a prospective cohort study. *J Nucl Med*. 2016;57:715–720.
- Antwi K, Fani M, Nicolas G, et al. Localization of hidden insulinomas with ⁶⁸Ga-DOTA-exendin-4 PET/CT: a pilot study. *J Nucl Med*. 2015;56:1075–1078.
- Normandin MD, Petersen KF, Ding Y-S, et al. In vivo imaging of endogenous pancreatic β -cell mass in healthy and type 1 diabetic subjects using ¹⁸F-fluoropropyl-dihydroetetrabenazine and PET. *J Nucl Med*. 2012;53:908–916.
- Carlsson L, Espes D, Lubberink M, et al. [¹¹C]5-hydroxy-tryptophan PET for assessment of islet mass during progression of type 2 diabetes. *Diabetes*. 2017;66:1286–1292.
- Bini J, Naganawa M, Nabulsi N, et al. Evaluation of PET brain radioligands for imaging pancreatic β -cell mass: potential utility of ¹¹C-(+)-PHNO. *J Nucl Med*. 2018;59:1249–1254.
- Diamant M, Van Gaal L, Stranks S, et al. Once weekly exenatide compared with insulin glargine titrated to target in patients with type 2 diabetes (DURATION-3): an open-label randomised trial. *Lancet*. 2010;375:2234–2243.
- Khera E, Zhang L, Roberts S, et al. Blocking glucagon like peptide-1 receptors in the exocrine pancreas improves specificity for beta cells in a mouse model of type 1 diabetes. *J Nucl Med*. 2019;60:1635–1641.
- Jodal A, Schibli R, Béhé M. Targets and probes for non-invasive imaging of β -cells. *Eur J Nucl Med Mol Imaging*. 2017;44:712–727.
- Brand C, Abdel-Atti D, Zhang Y, et al. In vivo imaging of GLP-1R with a targeted bimodal PET/fluorescence imaging agent. *Bioconjug Chem*. 2014;25:1323–1330.
- Clardy SM, Keliher EJ, Mohan JF, et al. Fluorescent exendin-4 derivatives for pancreatic β -cell analysis. *Bioconjug Chem*. 2014;25:171–177.
- Saudek F, Brogren C-H, Manohar S. Imaging the beta-cell mass: why and how. *Rev Diabet Stud*. 2008;5:6–12.
- Chen C, Cohrs CM, Stertmann J, Bozsak R, Speier S. Human beta cell mass and function in diabetes: RECENT advances in knowledge and technologies to understand disease pathogenesis. *Mol Metab*. 2017;6:943–957.
- Deán-Ben XL, Fehm TF, Ford SJ, Gottschalk S, Razansky D. Spiral volumetric optoacoustic tomography visualizes multi-scale dynamics in mice. *Light Sci Appl*. 2017;6:e16247.
- Schellenberg MW, Hunt HK. Hand-held optoacoustic imaging: a review. *Photoacoustics*. 2018;11:14–27.
- Knieling F, Neufert C, Hartmann A, et al. Multispectral optoacoustic tomography for assessment of Crohn’s disease activity. *N Engl J Med*. 2017;376:1292–1294.
- Regensburger AP, Fonteyne LM, Jüngert J, et al. Detection of collagens by multispectral optoacoustic tomography as an imaging biomarker for Duchenne muscular dystrophy. *Nat Med*. 2019;25:1905–1915.
- Neuschmelting V, Burton NC, Lockau H, et al. Performance of a multispectral optoacoustic tomography (MSOT) system equipped with 2D vs. 3D handheld probes for potential clinical translation. *Photoacoustics*. 2015;4:1–10.
- Roberts S, Strome A, Choi C, et al. Acid specific dark quencher QC1 pHILIP for multi-spectral optoacoustic diagnoses of breast cancer. *Sci Rep*. 2019;9:8550–8562.
- Roberts S, Andreou C, Choi C, et al. Sonophore-enhanced nanoemulsions for optoacoustic imaging of cancer. *Chem Sci*. 2018;9:5646–5657.
- Ishihara H, Asano T, Tsukuda K, et al. Pancreatic beta cell line MIN6 exhibits characteristics of glucose metabolism and glucose-stimulated insulin secretion similar to those of normal islets. *Diabetologia*. 1993;36:1139–1145.
- Glatz J, Deliolanis NC, Buehler A, Razansky D, Ntziachristos V. Blind source unmixing in multi-spectral optoacoustic tomography. *Opt Express*. 2011;19:3175–3184.
- Tzoumas S, Nunes A, Olefir I, et al. Eigenspectra optoacoustic tomography achieves quantitative blood oxygenation imaging deep in tissues. *Nat Commun*. 2016;7:12121.
- Ding L, Deán-Ben XL, Burton NC, Sobol RW, Ntziachristos V, Razansky D. Constrained inversion and spectral unmixing in multispectral optoacoustic tomography. *IEEE Trans Med Imaging*. 2017;36:1676–1685.
- Cheng K, Delghingaro-Augusto V, Nolan CJ, et al. High passage MIN6 cells have impaired insulin secretion with impaired glucose and lipid oxidation. *PLOS ONE*. 2012;7:e40868.

42. Johnson SP, Ogunlade O, Lythgoe MF, Beard P, Pedley RB. Longitudinal photoacoustic imaging of the pharmacodynamic effect of vascular targeted therapy on tumors. *Clin Cancer Res*. 2019;25:7436–7447.
43. Chan DXH, Sugii S, Han W. A UCPI near-infrared reporter system for monitoring adipose “browning” in vivo using photoacoustic imaging [abstract]. *Diabetes*. 2018;67(suppl):280.
44. Krumholz A, Wang L, Yao J, Wang LV. Functional photoacoustic microscopy of diabetic vasculature. *J Biomed Opt*. 2012;17:060502.
45. Sim JY, Ahn C-G, Jeong E-J, Kim BK. In vivo microscopic photoacoustic spectroscopy for non-invasive glucose monitoring invulnerable to skin secretion products. *Sci Rep*. 2018;8:1059–1070.
46. Weiss R, Yegorchikov Y, Shusterman A, Raz I. Noninvasive continuous glucose monitoring using photoacoustic technology: results from the first 62 subjects. *Diabetes Technol Ther*. 2007;9:68–74.
47. Feng W, Shi R, Zhang C, Liu S, Yu T, Zhu D. Visualization of skin microvascular dysfunction of type 1 diabetic mice using in vivo skin optical clearing method. *J Biomed Opt*. 2018;24:1–9.
48. Yagihashi S. Clinical application of photoacoustic imaging to the evaluation of diabetic polyneuropathy [abstract]. *Diabetes*. 2018;67(suppl):582.
49. Zhang L, Thurber GM. Quantitative impact of plasma clearance and down-regulation on GLP-1 receptor molecular imaging. *Mol Imaging Biol*. 2016;18:79–89.
50. Chintinne M, Stangé G, Denys B, Ling Z, In 't Veld P, Pipeleers D. Beta cell count instead of beta cell mass to assess and localize growth in beta cell population following pancreatic duct ligation in mice. *PLoS One*. 2012;7:e43959.
51. Manandhar B, Ahn J-M. Glucagon-like peptide-1 (GLP-1) analogs: recent advances, new possibilities, and therapeutic implications. *J Med Chem*. 2015;58:1020–1037.